# Ring formation in nanoliter cups: Quantitative measurements of flow in micromachined wells

B. Rieger, L. R. van den Doel, and L. J. van Vliet*
*Pattern Recognition Group, Delft University of Technology, Lorentzweg 1, NL-2628 CJ Delft, The Netherlands*
(Received 12 March 2003; published 26 September 2003)

Drying of DNA spots on microarrays and spilled coffee yields ringlike stains, because the outward flow transports dissolved particles to the border. Contact line pinning and diffusion limited evaporation of a liquid sample are the two necessary conditions to induce an outward directed liquid flow during evaporation. In this paper we present quantitative measurements of this flow field visualized by microspheres which are injected into a liquid sample in circular wells with a radius of 100–150 $\mu$m and a depth of 6 $\mu$m. The motion, including Brownian motion, of these microspheres with a radius of 0.25 $\mu$m is recorded using digital fluorescence microscopy. Our analysis, using optic flow, does not require object identification, nor tracking of the individual objects. The spatiotemporal measurement space is sparsely filled at only those space/time positions where a microsphere is present. A confidence measure is computed indicating the presence of microspheres in this measurement space. The circular well shape allows us to transform the sparse measurement space into a denser, averaged radial velocity field. In this transformation we ''interpolate'' the radial velocity between values with a high confidence, which results in quantitative measurements of this outward flow field during the complete time interval of the evaporation process and at all radial positions in the circular wells. This allows for a quantitative validation of the elegant theory of ring formation.

DOI: 10.1103/PhysRevE.68.036312 PACS number(s): 47.55.Dz, 47.15.Gf, 87.64.Rr, 87.57.Nk

## I. INTRODUCTION

Evaporation of liquid samples is a key problem in the development of microarray technology (including labs-on-a-chip), especially in the case of open reactors. We have studied the process of evaporation in micromachined sub-nanoliter wells with a typical radius of 75–150 $\mu$m and a typical depth of 6 $\mu$m using interference-contrast microscopy [1,2]. With this microscope-based technique dynamic fringe patterns, showing fringes of equal height, can be observed. Since the depth of the well is only 6 $\mu$m, the liquid sample can be regarded as a thin film and the fringe patterns are Newton rings. From these fringe patterns the shape of the air-liquid interface can be retrieved using a temporal phase-unwrapping technique [2]. The rate of change of these dynamic height profiles represents the *total* evaporation rate of the liquid in the sub-nanoliter well. We have found that the total evaporation rate is linearly proportional to the perimeter of the well [2]. We will present these experimental results in the following section. This counterintuitive result is a consequence of diffusion-limited evaporation. In the following section, we will briefly repeat the most important results of this theory.

The theory of diffusion-limited evaporation predicts an outward directed flow in a droplet, which transports dissolved particles to the perimeter of the droplet, a phenomenon responsible for ringlike stains on flat surfaces: this is the explanation for the formation of coffee rings [3,4]. In macroscopic droplets this evaporation induced flow field has been coarsely sampled by tracking microspheres only near the edge of the droplet and only at the end of the evaporation process [4]. On the basis of this theory we expected a similar outward directed liquid flow in our wells, but this flow could not be observed with interference-contrast microscopy. In order to visualize this flow field and to validate the theory of ring formation, we conducted experiments in which sub-nanoliter wells were filled with a liquid in which fluorescent microspheres were introduced. The motion, including Brownian motion, of the microspheres (radius 0.25 $\mu$m) during evaporation of the liquid sample was monitored using digital fluorescence microscopy. The acquired digital recordings (image sequences) clearly showed the transportation of the microspheres to the perimeter of the well. Figure 1(a) shows the distribution of the fluorescent microspheres right after injection of the mixture in the well. Figure 1(b) shows the trajectories of the dissolved microspheres during evaporation. All trajectories point outward, when observed over a long time ($\approx$3 min). When observed on a finer time scale ($\approx$seconds), the random behavior due to Brownian motion is clearly visible, but only in the early stage of the evaporation process. Figure 1(c) shows the microspheres almost at the end of the evaporation process; practically all microspheres have been transported to the edge of the well.

In this paper, we present quantitative measurements of the entire outward directed flow field: during the complete time interval of the evaporation and at all radial positions. First, we summarize the most important aspects of diffusion-limited evaporation regarding droplets. We will argue that these aspects are applicable to our nanoliter wells. Second, we will discuss in detail the effects of the liquid flow on the microspheres. Third, we will present a digital image analysis approach, using optic flow, to measure the flow field. Our approach requires neither object identification nor tracking of the individual objects. As the well contains a limited number ($\approx$180) of microspheres, we obtain a sparse spatiotemporal measurement space. The local velocity (flow field) and a confidence value is computed from this measurement space. The confidence is high at $(x,y,t)$ positions where a sphere is present and low elsewhere. The confidence map allows for a

*Electronic address: {bernd,richard,lucas}@ph.tn.tudelft.nl

 

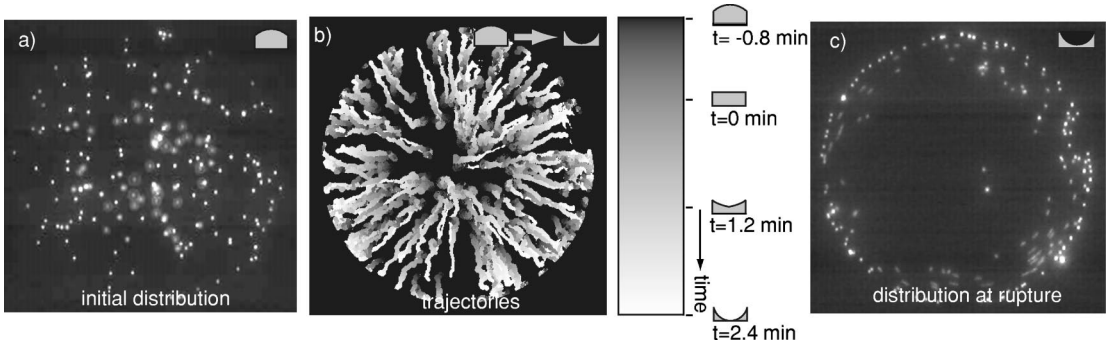


FIG. 1. Image (a) shows the distribution of the microspheres (radius 0.25 $\mu$m) directly after filling the circularly shaped well (radius 100 $\mu$m) with an evaporating ethylene glycol sample. Image (b) shows the trajectories of the fluorescent beads. The gray-scale map represents time. Image (c) shows the distribution of the microspheres just before the meniscus (air-liquid interface) touches the ground in the middle of the well and breaks. The instant $t=0$ corresponds to the moment that the meniscus is perfectly flat. The corresponding meniscus shape is illustrated next to the gray-scale map.

transformation of the flow field $\vec{v}(x,y,t)$ into an estimate of the radial velocity $\hat{v}(r,t)$ as a function of the radial position $r$ and time $t$. Finally, we will compare the measured flow field with the predicted flow field.

## II. DIFFUSION-LIMITED EVAPORATION

Recently, the formation of ring stains in ''macroscopic'' droplets, e.g., coffee droplets, was explained by Deegan *et al.* as the result of contact line pinning at the edge of the droplet, and evaporation-limited diffusion of molecules from the saturated vapor layer to the environment [3,4]. These two conditions are responsible for the outward directed flow and explain our observations of the transportation of the fluorescent microspheres as shown in Fig. 1.

Deegan *et al.* state that the rate limiting step of the evaporation process determines the functional form of the local evaporation rate $j(r)$ along the air-liquid interface. If the evaporation process is *diffusion* limited, then the diffusion process will rapidly attain a steady state: the diffusion equation reduces to the Laplace equation. This results in a boundary value problem with boundary conditions $u=u_s$ (saturated vapor pressure) at the interface and $u=u_\infty$ (ambient vapor pressure) far away from the interface, which can be solved analytically, under the assumption that the shape of the droplet is a spherical cap. Deegan *et al.* verified experimentally that a spherical cap describes the shape of the air-liquid interface of a droplet [4]. If the footprint of the droplet has a constant radius $R$ and the height in the center of the droplet is $H(t)$ as a function of the time $t$, then it is straightforward to derive that the height $h(r,t)$ of the interface at a distance $r$ from the center of the droplet is given by

$$h(r,t)=\frac{H^2(t)-R^2}{2H(t)}+\frac{\sqrt{H^4(t)-4H^2(t)r^2+2H^2(t)R^2+R^4}}{2H(t)}. \tag{1}$$

Deegan *et al.* give a very good approximation for the analytical solution of the boundary value problem given the geometry of the droplet defined in Eq. (1):

$$j(r)\propto\frac{1}{\sqrt{1-\left(\frac{r}{R}\right)^2}}. \tag{2}$$

Equation (2) shows that the evaporation rate is strongly enhanced towards the edge of the droplet. As a result, the loss of liquid at the edge due to evaporation must be replenished by liquid from the bulk of the droplet. This induces an outward directed liquid flow $v(r,t)$.

Given the expressions for the dynamic height of the air-liquid interface of the droplet $h(r,t)$ [Eq. (1)], the (static) local evaporation rate $j(r)$ [Eq. (2)], and the rate of change of the height in the center of the droplet, the outward flow field $v(r,t)$ as a function of the radial position $r$ and time $t$ follows from a mass balance [4]:

$$v(r,t)=-\frac{1}{\rho r h}\int_0^r dr' r'\left\{j(r')\sqrt{1+\left(\frac{\partial h}{\partial r'}\right)^2}+\rho\frac{\partial h}{\partial t}\right\}, \tag{3}$$

with $\rho$ the liquid density. From this equation it is clear that a nonzero $v$ arises when there is a mismatch between the local evaporation rate $j(r)$ and the rate of change of the height profile $h(r,t)$.

There are three differences between our experiments and the experiments of Deegan *et al.* First, the geometry of the liquid sample in our circular wells differs from the geometry of a droplet on a flat surface. The shape of the air-liquid interface is measured using interference-contrast microscopy [1,2]. With this microscope-based technique, fringe patterns showing Newton rings are generated. The depth of the wells is only 6 $\mu$m and the liquid sample in the well can therefore be regarded as a thin film. Analysis of the fringe patterns acquired by interference-contrast microscopy results in the height profile of the meniscus as a function of time [2]. Figure 2 shows nine (out of a large series) retrieved height profiles (solid lines) of the air-liquid interface as a function of the radial position. The time difference between two succes-

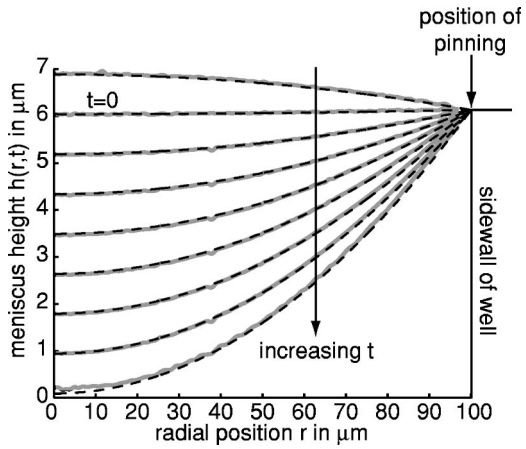


FIG. 2. The measured height profiles of the meniscus (solid lines) and height profiles representing spherical caps (dashed lines) obtained by fitting as a function of evaporation time.

sive profiles is 20 s. The dashed lines show the height profiles computed from Eq. (1) with $R=100\ \mu$m and the best fit to the center,

$$H(t)=(7.38\ \mu\text{m}-6.13\ \mu\text{m})-(0.042\ \mu\text{m/s})t. \qquad (4)$$

The depth of the well (estimated value 6.13 $\mu$m) is added to $h(r,t)$ to compute the height of the air-liquid interface with respect to the bottom of the well. The expression for $H(t)$ follows from fitting a first-order polynomial to the measured heights of the air-liquid interface in the center of the well. Figure 2 confirms that the meniscus can be modeled by spherical caps. In other words: Eq. (1) is valid for the air-liquid interface of the liquid sample in our wells.

Second, we have used ethylene glycol for our experiments rather than water. The evaporation process is extended to a time scale on the order of a few minutes instead of a few seconds. With the technique of interference-contrast microscopy we have found that the total evaporation rate for a circular well is constant in time [2]. Figure 3 shows the remaining liquid volumes for different sized circular wells as a function of time during evaporation. The slope of these

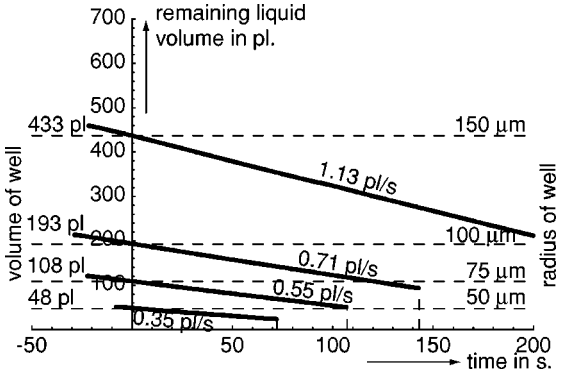


FIG. 3. The solid lines show the remaining liquid volume in different sized circular wells as a function of time. The slope of these lines defines the total evaporation rate. The fact that these are lines indicates that the total evaporation rate as a function of time is constant.

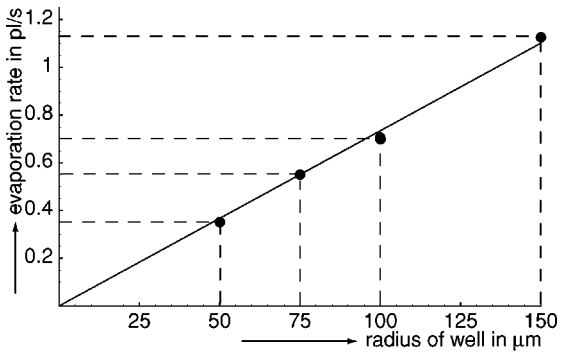


FIG. 4. This graph shows that there is a linear relation between the total evaporation rate and the radius $R$ of the well. This implies that the evaporation process is diffusion limited.

straight lines is the total evaporation rate. From these graphs we conclude that the total evaporation rate is constant in time. A second conclusion is that any thermal effect, cooling of the liquid due to evaporation, is negligible. The large silicon volume in which the well is fabricated is a source of thermal energy that can easily compensate for any loss of thermal energy due to evaporation, especially since the evaporation is such a slow process. Furthermore, the total evaporation rate as a function of the well radius $R$ can be calculated from the graphs in Fig. 3. Figure 4 shows this relation. The linear dependency of the total evaporation rate on the radius of the well implies that the evaporation process in our wells is indeed diffusion limited.

Third, at the start of our experiment, the meniscus is convex and the geometry of the meniscus is identical to the geometry of a droplet on a flat surface. The fact that we have a cylindrical liquid volume with a radius $R$ and a depth of 6 $\mu$m is *not* important for the boundary value problem to be solved. No molecules can escape via the bottom or via the side walls of the well, just as no molecules can escape through the footprint of a droplet on the surface. At the start of our experiment, we have the same geometry as Deegan *et al.*, the same type of diffusion process, the same boundary value problem, and therefore the same form of the local evaporation rate. In other words, at the start of our experiment Eq. (2) is valid. Furthermore, since a diffusion-limited evaporation process implies a static local evaporation rate [4], we conclude that this form is valid during the entire evaporation process, where the meniscus changes from convex via flat to concave until the meniscus breaks at the bottom of the well. Figures 3 and 4 support this conclusion, i.e., $j(r,t)=j(r)$.

Considering the three differences described above, we can still use the expressions for the dynamic height of the air-liquid interface of the droplet $h(r,t)$ [Eq. (1)], the (static) local evaporation rate $j(r)$ [Eq. (2)], and the rate of change of the height in the center of the well [Eq. (4)]. The outward flow field $v(r,t)$ as a function of the radial position $r$ and time $t$ follows from Eq. (3).

Figure 5(a) shows the flow $v(r,t)$ for a circular well (radius 100 $\mu$m, depth 6.13 $\mu$m) according to Eq. (3). As can be seen in this figure, the flow in the initial phase of the evaporation is very slow ($\approx 0.1\ \mu$m/s). At the end of the

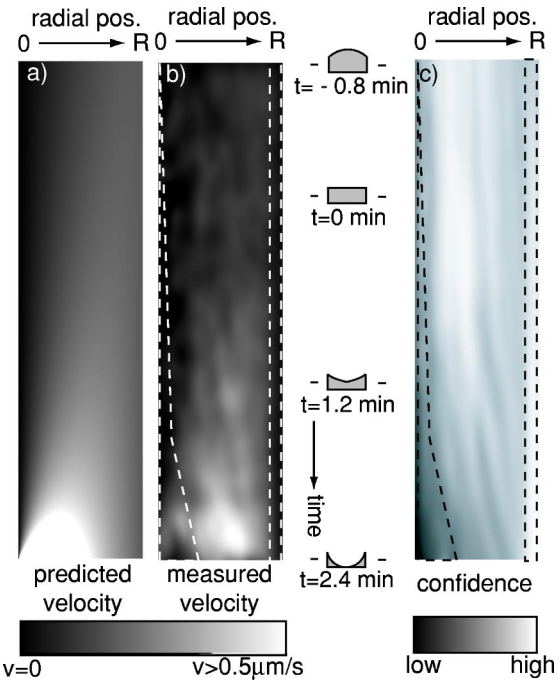


FIG. 5. Image (a) shows the predicted outward-directed flow field $v(r,t)$ as a function of time $t$ and radial position $r$. Image (b) shows the measured outward-directed flow field $\hat{v}(r,t)$. Image (c) shows the radial confidence field $\hat{c}(r,t)$. The instant $t=0$ corresponds to the moment that the meniscus is perfectly flat. In the dashed region for small radial positions the confidence is very low, because of the absence of microspheres. In the dashed region for large radial positions, the microspheres at rest do not represent the flow.

evaporation process the velocity of the flow increases [$\approx 1$ $\mu$m/s, in Fig. 5(a) the velocity is clipped at 0.5 $\mu$m/s for good visualization]. Due to symmetry the velocity in the center of the well is zero at all instants. Note that the theory predicts that the flow at the edge of the well is *not* zero. Furthermore, the form of the local evaporation rate in our wells is identical to the form in the case of droplets. The flow field in our wells, however, is *not* identical to the flow field in a droplet. The difference is the 6-$\mu$m-deep cylindrical volume in our wells. This keeps the flow field at the edge of the well at some finite value, whereas in the case of a droplet, the flow field at the edge of the droplet diverges (mathematically).

Figure 2 suggests that the change of the shape of the air-liquid interface is significant. This is, however, *not* the case. The well is only 6 $\mu$m deep, small compared to the radius of the well, $R=150$ $\mu$m, which yields a meniscus that is practically flat during the complete process of evaporation.

### III. MOTION OF MICROSPHERES IN THE FLUID

In this section, we will discuss whether the microspheres are well suited to monitor the flow. The first question is: are the spheres small enough, not to influence the flow and to represent it accurately? Second, are they big enough, such that Brownian motion is not a major effect? Finally, is the diameter of the spheres small enough compared to the depth of the well?

(1) The outward directed flow is laminar, since the Reynolds number $\mathrm{Re}=\rho v l/\eta \ll 1$, with $l$ a characteristic length, i.e., the radius of the microspheres, $v \approx 1$ $\mu$m/s the velocity, $\eta = 16.1\times 10^{-3}$ Pa s the viscosity of ethylene glycol at 298 K, and $\rho = 1.1\times 10^{3}$ kg/m$^3$ the density of ethylene glycol. Stokes's law gives the friction force on a microsphere as

$$F = 6\pi r \eta (v - v_k), \tag{5}$$

with $v$ the velocity of the fluid and $v_k$ the velocity of the sphere. From this follows the acceleration of the sphere as $\dot{v}_k = C(v - v_k)$ with $C = 9\eta/2\rho_k r_k^2$, with $\rho_k = 905$ kg/m$^3$ the density of the microspheres (polypropylene). The velocity of the fluid changes very slowly in time. Consequently, we assume $v$ to be constant and obtain

$$v_k(t) = v(1 - e^{-Ct}), \quad C = 8\times 10^{-5} \times \frac{1}{r_k^2}\frac{\mathrm{m}^2}{\mathrm{s}} \tag{6}$$

as the solution of the equation of motion with boundary condition $v_k(0)=0$. For $r_k = 0.25$ $\mu$m we conclude that $v_k \rightarrow v$ instantaneously. Whereas if the constant $C$ were on the order of unity (for $r_k \approx 5$ mm), the time to reach $v_k = 0.95v$ starting from initial rest would then be $\approx 5$ s.

(2) The average quadratic displacement in three dimensions of a microsphere due to Brownian motion in a static solution in a time interval $t$ is given by $\langle x^2 \rangle = 6Dt$, with $D$ the diffusion constant defined by the Einstein relation [5]

$$D = \frac{k_B T}{6\pi \eta r_k}. \tag{7}$$

In our experimental setup we only observe the projected two-dimensional (2D) displacement $\sqrt{\langle x_{ob}^2 \rangle}$ rather than the real 3D displacement $\sqrt{\langle x^2 \rangle}$. Their relation is given by the stereological factor, the average projected displacement of all 3D displacements,

$$\sqrt{\langle x_{ob}^2 \rangle} = \frac{\int_0^1 \sqrt{1-z^2}\,dz}{\int_0^1 dz}\sqrt{\langle x^2 \rangle} = \frac{\pi}{4}\sqrt{\langle x^2 \rangle}. \tag{8}$$

Finally, we obtain $\langle x_{ob}^2 \rangle = \frac{3}{8}\pi^2 Dt \approx 3.7Dt$. Recall that $\langle x^2 \rangle = 4Dt$ for 2D Brownian motion. With the values for $\eta$ and $r_k$, we have $D = 0.054$ $\mu$m$^2$/s. In the early stage of the evaporation $v \approx 0.1$ $\mu$m/s and we conclude that Brownian motion is a significant effect, but Brownian motion becomes negligible towards the end of the evaporation process with $v > 1$ $\mu$m/s.

(3) The choice for microspheres with a radius of 0.25 $\mu$m seems reasonable, given the depth of our wells (6 $\mu$m). The particles are small enough that they immediately drift with the flow. Smaller particles would be more influenced by Brownian motion. Larger particles would reduce the contribution of Brownian motion, but larger particles would strand

at the bottom of the well early in the evaporation process when the fluid level in the middle of the well decreases.

### IV. IMAGING MICROSPHERES IN THE FLUID

In the preceding section we argued that the microspheres were suited to visualize the flow from a transportation point of view. In this section we will discuss if the microspheres can be imaged properly onto a detector and recorded, such that the analysis of the acquired image sequence results in a good description of the liquid flow. Figure 1(a) clearly shows that not all microspheres are in focus. Right below the center of the well in Fig. 1(a) some out-of-focus microspheres can be seen; instead of a small bright spot, a bright and dark ring can be seen around a dimmer spot. In microscopy the following approximation is used to describe the depth of focus for a quarter of a wavelength defocus error [6]:

$$(\text{depth of focus}) = \frac{\lambda}{4n\left(1-\sqrt{1-\frac{N_{A^2}}{n^2}}\right)}, \qquad (9)$$

with $\lambda = 605$ nm the emission wavelength of the Rhodamine-stained microspheres, $n = 1.43$ the refractive index of ethylene glycol, and $N_A = 0.75$ the numerical aperture of the objective used for microscopic imaging. This is the maximum tolerance of defocusing without significant distortion of the image (which is in fact the $\lambda/4$ criterion for the wave front distortion of the marginal ray of the lens). Inserting these values in Eq. (9) yields a total depth of focus [defocusing error $|\Delta z| < (5/4)\lambda$] of 1.5 $\mu$m. If we position the focal plane at half the depth of our wells, then the 6 $\mu$m depth of the wells implies a maximum defocusing error of one wavelength disregarding evaporation. The out-of-focus microspheres in Fig. 1(a) may very well have this defocusing error. In our experiments, we have positioned the focal plane below half the depth of the wells, since the height of the liquid decreases during the evaporation process. This implies that during the evaporation process the out-of-focus microspheres tend to move in focus. This can be seen in Fig. 1(c), where practically all microspheres are sharply imaged. The unsharpness in Fig. 1(c) is due to very fast motion at the instant when the meniscus hits the bottom of the well.

Any analysis that requires sharply imaged objects, such as segmentation and tracking of objects, as used by Deegan *et al.* [4], can only be applied in a short time interval and for small changes in the height of the air-liquid interface. The technique we propose takes these intensity fluctuations due to defocusing into account. Consequently, we can measure the flow field during the complete course of evaporation and at all radial positions.

### V. IMAGE ANALYSIS OF DIGITAL RECORDINGS

In this section we will present a gray-level based image analysis approach to estimate the average radial velocity of the microspheres in the fluid. This approach does *neither* require segmentation *nor* tracking of the individual microspheres.

One option to measure the flow is standard particle image velocimetry (PIV) [7]. PIV is used for monitoring and analyzing laminar and turbulent flow behavior mainly in pipes, based on the cross correlation of subsequent images. PIV assumes that *many* tracer particles are *uniformly* distributed in the fluid. Computation of the local shift between two successive images requires at least one particle to be present in the interrogation window. For an image with a size of about $218 \times 218$ $\mu$m$^2$ [Fig. 1(a)] and about 180 visible dissolved microspheres, the correlation window must be at least $16 \times 16$ $\mu$m$^2$. Note that the estimation of the correlation peak from one marker is not very robust. Furthermore, the flow is not expected to be uniform in larger windows, but radially diverging from the center of the well. Therefore we conclude that we do not satisfy the assumptions necessary for robust velocity estimation via PIV. The use of more markers in this micron scale flow study results in indistinguishable objects after imaging. Smaller microspheres do not emit sufficient light for a reasonable signal-to-noise ratio. The average shift of a microsphere between two successive images in our experiments is small (0.01–0.07 pixel units) and PIV with subpixel interpolation can only obtain measurements with an uncertainty of 0.1 pixel units [8]. Another possibility is to leave out several images in the sequence and compute the cross correlation between them. This is not necessary in our approach, therefore we can use all available images for improving the signal-to-noise ratio allowing high precision velocity estimation.

A second option to measure the flow field is segmentation of the microspheres and tracking over the course of the fluid evaporation. This is not very promising. As discussed earlier, we see all microspheres in a projection. Not all microspheres are in the focal plane, therefore some of the microspheres appear blurred. This makes segmentation a difficult task, which can be avoided by our gray-value approach.

The technique we propose uses *optic flow* [9]. It computes the velocity per pixel for the whole image sequences $I(x,y,t)$. The trajectories of the microspheres form spaghettilike structures in $I(x,y,t)$, see Fig. 6. Where PIV uses only two successive images to compute the shift of the tracers, optic flow uses more images. Velocity is interpreted as orientation in the spatiotemporal image sequence. The use of several images simultaneously yields a higher precision and accuracy for the velocity estimate. Optic flow starts from the assumption that the intensity per object, $I(\vec{x},t)$ is conserved, such that

$$I(\vec{x},t) = I(\vec{x}+d\vec{x},t+dt). \qquad (10)$$

Assuming a uniform rectilinear motion $\vec{v} = \text{const}$, we can use a first-order Taylor expansion of the right-hand side of Eq. (10), $I(\vec{x}+d\vec{x},t+dt) = I(\vec{x},t) + \vec{\nabla} I(\vec{x},t) \cdot \vec{v} + \partial_t I(\vec{x},t)$, with $\vec{\nabla} = (\partial_x, \partial_y)$, and combine it with Eq. (10). This yields the well-known flow equation

$$\vec{\nabla} I \cdot \vec{v} + \partial_t I = 0. \qquad (11)$$

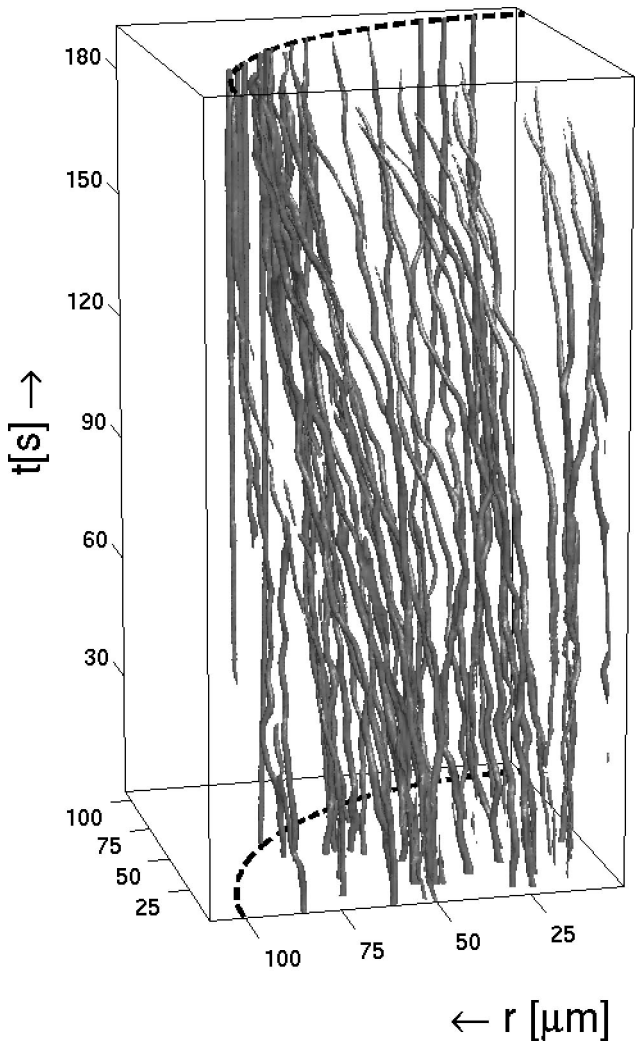


FIG. 6. Isosurface plot of the trajectories of microspheres in a quarter of the well after 1D adaptive filtering. The time axis points upwards and we only show every seventh time frame of the $(x,y,t)$ image.

Equation (11) is a scalar equation, which does not allow the computation of all components of $\vec{v}$. This is known as the aperture problem. Expanding the constraint of constant velocity to a small neighborhood $V=(\Delta\vec{x},\Delta t)$, introduced first by Lucas and Kanade [9], we can solve Eq. (11) for $\vec{v}$ using a least squares approach:

$$\vec{v}(x,y,t)=-\frac{1}{V^2}\int dV(\vec{\nabla}I\vec{\nabla}I^t)^{-1}\int dV\vec{\nabla}I\partial_t I. \qquad (12)$$

The images are recorded with a charge-coupled device (CCD) camera and processed with a computer; thus we deal with discrete signals rather than continuous functions. Equation (12) therefore requires discrete derivatives. Finite differences of image values divided by the pixel distance is not the ideal derivative for images [10,11]. Gaussian derivative filters (or at least approximations) are used ordinarily in image processing as they combine noise suppression and localization in an optimal way [10,11]. A discrete derivative is computed with the help of a regularized derivative, as in distribution theory, i.e., using a convolution of the image with derivatives of Gaussians characterized by their standard deviation $\sigma$. The parameter or scale $\sigma$ defines the smoothing. A larger $\sigma$ results in a higher noise suppression and blurring. The effective width of a Gaussian filter is $(-3\sigma,3\sigma)$. Equation (12) involves three scales: the spatial derivatives $\vec{\nabla}(\sigma_g)$, the temporal derivative $\partial_t(\sigma_t)$, and the averaging in $V(\sigma_T)$. We have set $\sigma_g=0.52$ $\mu$m, $\sigma_t=0.2$ s, and $\sigma_T=(2.6\ \mu\text{m},0.3\text{ s})$. The reason for these choices is as follows: $\sigma_g$ should be small enough to detect abrupt changes in intensity transitions from the background intensity level to the object level. We want a standard deviation of $\sigma_t=0.2$ s to average over several ($\approx 18$) successive images. The regularization kernel $\sigma_T$ has to be large since the structure is estimated in a spatiotemporal neighborhood defined by $\sigma_T$. Our velocity estimation is not critically dependent on the choice of the scale parameters, i.e., no fine tuning is needed. A range of values will only lead to very small changes in the estimated velocity.

Given the lowering of the meniscus during the evaporation, the changes of the focal plane, and the Brownian motion in the axial direction, the microspheres drift in and out of focus. This causes a varying recorded intensity per microsphere, which is not compatible with the assumption of optic flow. An adaptive 1D filter along the trajectories is applied before computing the optic flow to suppress noise and to reduce the intensity variations without spurious blurring of the image [12]. Figure 6 shows the trajectories in a quarter of the well after preprocessing. Adaptive filtering requires knowledge about the local structure in the image in order to adapt to it. The orientations of the trajectories of the microspheres are estimated by an eigenvalue analysis of the gradient structure tensor [13]. This is a generic tool to estimate the local structure and the dimensionality of the structure in images. The gradient structure tensor is closely related to the inertia tensor from classical mechanics. For linelike structures the eigenvector associated with the smallest eigenvalue corresponds to the orientation of the trajectory and the eigenvalues are distributed as $\lambda_1\approx\lambda_2\gg\lambda_3$. Furthermore, this permits the computation of a robust normalized confidence field

$$c(x,y,t)=\frac{\lambda_2-\lambda_3}{\lambda_2+\lambda_3}, \qquad (13)$$

where $c\approx 1$ for lines in the spatiotemporal image and zero elsewhere.

After adaptive filtering and optic flow estimation, the radial velocity needs to be estimated against fluctuations of individual particle movements. The limited number of particles results in a $(x,y,t)$ image that is sparsely filled with trajectories. As a consequence, the velocity field $\vec{v}(x,y,t)$ only contains reliable data along/near the trajectories, i.e., $(x,y,t)$ locations with high confidence. This is especially the case in the center of the well near the end of the evaporation process, since most of the microspheres that were present in the center at the start of the experiment have been displaced

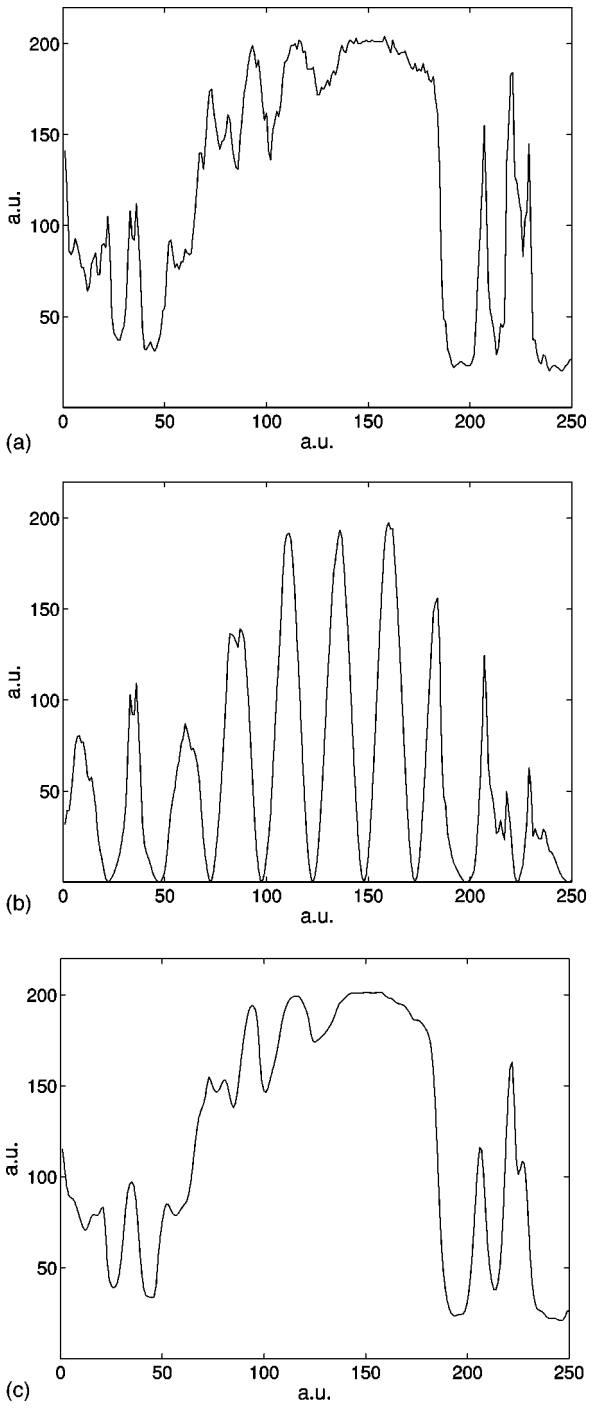


FIG. 7. Demonstration of interpolation using normalized convolution; (a) original signal $s$, (b) signal confidence product $s \cdot c$ with some confidence $c \in [0,1]$, and (c) reconstructed signal $(s \cdot c) * w / c * w$ with a Gaussian weight function $w$, where * is the convolution operator.

to the border of the well by the liquid flow. In regions with low confidence (few or no microspheres present) the velocity can be estimated by normalized convolution [13], which interpolates the signal between parts of high confidence. See Fig. 7 for an example of the use of normalized convolution for interpolation purposes.

The circular shape of our well justifies angular averaging

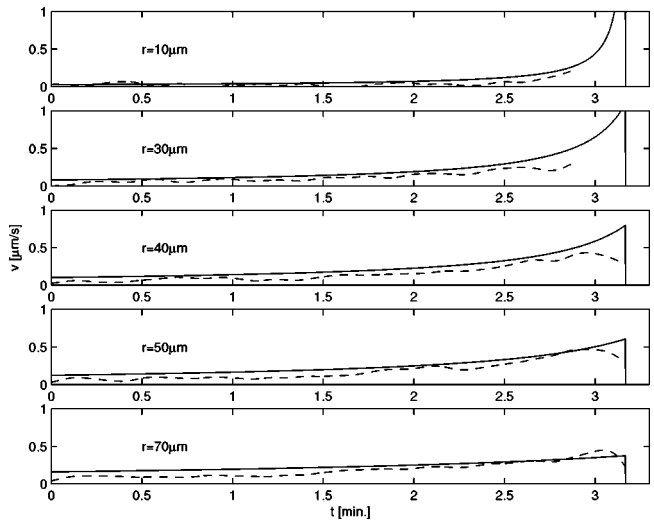


FIG. 8. Theoretical (solid line) and estimated velocity $\hat{v}$ (dashed line) for different radii as a function of time. The radius of the well is 100 $\mu$m.

of the radial components of the velocities. Given the velocity field $\vec{v}(x,y,t)$, averaging over all measurements in a ring between radii $r$ and $r+dr$ results in a more robust estimate of $v(r,t)$ and interpolation between measurements with high confidence compensates for the sparse field. The averaging and interpolation are performed simultaneously. This requires the radial component of the velocity field to be weighted with the confidence field, or $v_r(x,y,t) = [\vec{v}(x,y,t) \cdot \hat{r}] c(x,y,t)$ with $\hat{r} = \vec{r}/|r|$. The combination of radial averaging and spatiotemporal interpolation on measurements with high confidence uses the weight function $w(x,y,t;r)$, which is a ring in the $xy$ plane that has a Gaussian profile, the center point at the center of the well $(x_0, y_0, t)$, and radius $r$:

$$w(x,y,t;r) = e^{-(1/2\sigma_{xy}^2)(\sqrt{(x-x_0)^2+(y-y_0)^2}-r)^2} e^{-t^2/2\sigma_t^2}, \tag{14}$$

where the temporal blurring is chosen to be much larger (in image pixels) than the spatial blurring as the predicted velocity is very smooth along the time dimension, i.e., $\sigma_t \gg \sigma_{xy}$. This weight function is applied to the velocity field as well as to the confidence field. The ratio of the two weighted fields gives an estimation for the flow field at radius $r$:

$$\hat{v}(r,t) = \frac{\sum_{x,y,\tau} v_r(x,y,\tau) w(x,y,t-\tau;r)}{\sum_{x,y,\tau} c(x,y,\tau) w(x,y,t-\tau;r)}. \tag{15}$$

The operation with the weight function in Eq. (15) is a scalar product in space and a convolution in time. The radial confidence field follows as

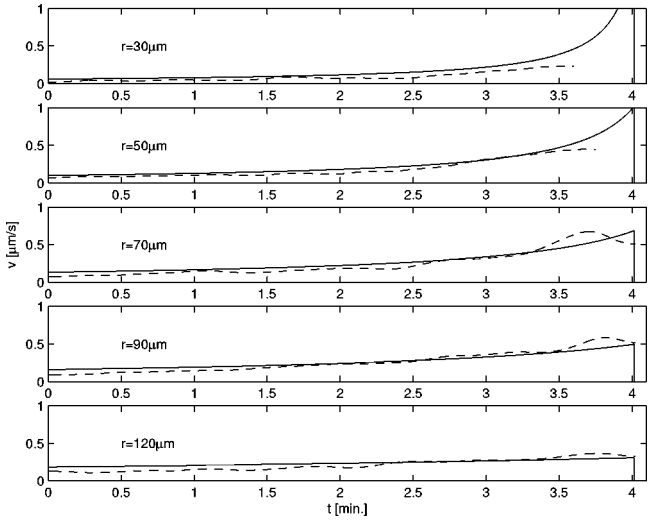


FIG. 9. Theoretical (solid line) and estimated velocity $\hat{v}$ (dashed line) for different radii as a function of time. The radius of the well is 150 $\mu$m.

$$\hat{c}(r,t)=\frac{\sum_{x,y,\tau} c(x,y,\tau)w(x,y,t-\tau;r)}{\sum_{x,y,\tau} w(x,y,t-\tau;r)}. \tag{16}$$

Figure 5(b) shows the computed radial velocity distribution $\hat{v}(r,t)$. Figure 5(c) represents the confidence $\hat{c}(r,t)$. In order to compare the predicted flow field with the computed flow field, we plot them for different radii in a well with a radius of 100 $\mu$m as shown in Fig. 8. Figure 9 shows the same comparison for a well with a radius of 150 $\mu$m. The estimated velocity $\hat{v}$ corresponds well with the predicted velocity, given the fact that the estimate is based on sparse measurements. The microspheres move towards larger radii during the evaporation and make the center of the well empty. This empty region grows during the evaporation process. Thus, for small radii, it is practically impossible to measure the velocity for $t \gg 0$. This explains the region with low confidence in the lower left corner (small radial position at the end of the experiment) in Fig. 5(c). For large radial positions, at the side wall of the well, the spheres will collide against the wall, stop moving, and no longer represent the flow.

## VI. DISCUSSION AND CONCLUSION

In this paper we present a method to measure the flow induced by an evaporating liquid sample in circular wells ($R=100$ $\mu$m, 150 $\mu$m, depth$=6$ $\mu$m) and compare the estimated flow field with the predicted flow field. The outward directed flow is a consequence of the pinning of the liquid at the edge of the well in combination with the diffusion-limited evaporation. Small ($r_k=0.25$ $\mu$m) microspheres are used to visualize the flow. The Brownian motion of the microspheres is only of influence in the very early stages of the evaporation when the flow velocity is small. We use optic flow to process the acquired image sequence and retrieve an estimate of the flow field (velocity image). Together with a confidence measure we are able to interpolate the relatively sparse measurement points in a generic manner. The final estimate of the radial velocity $\hat{v}(r,t)$ is in good agreement with the theoretical prediction, except at the side walls of the well.

Previous measurements of flow in droplets to support the theory have been limited to a small number of points in the lower right region of Fig. 5(b). The approach described here, which allows us for a detailed quantitative verification of the elegant theory of ring formation in pinned droplets (and wells), significantly outperforms the earlier presented results, which were based on coarse sampling by tracking microspheres only near the edge of macroscopic droplets and only at the end of the evaporation process [4].

## ACKNOWLEDGMENTS

The authors would like to acknowledge Professor J. G. Korvink from the Albert Ludwigs University in Freiburg, Germany, and Dr. K. T. Hjelt currently at Nokia, Helsinki, Finland for their stimulating discussions in the early stage of this research. Dr. ir. M. van Ginkel is acknowledged for supporting us with the image analysis and Professor I. T. Young for his help in preparing the final version of this manuscript. Both are from the Pattern Recognition Group of the Delft University of Technology. This work was partially supported by the Delft Interfaculty Research Center *Intelligent Molecular Diagnostic Systems* and the Netherlands Organization for Scientific Research NWO Grant No. 612-012-003.

## APPENDIX: METHODS AND MATERIALS

A small volume of Rhodamine-stained microspheres (Fluospheres, Molecular Probes, Leiden, The Netherlands, excitation wavelength 580 nm and emission wavelength 605 nm) with a radius of 0.25 $\mu$m was added to a droplet of pure ethylene glycol. This solution was mixed to get a uniform distribution of the microspheres. An Eppendorf Transjector 5246 (Eppendorf, Netheler-Hinz GmbH, 22331 Hamburg, Germany) was used to manually inject this mixture into the wells. A Femtotip II of which the tip was carefully removed to pass the spheres with 0.25 $\mu$m radius, was used as capillary. The experiments were performed on a Zeiss Axioskop microscope with a $20\times/0.75$ FLUAR objective and a fluorescence filter set from Zeiss (filter set no. 15, excitation, BP 546/12; beam splitter FT 580, emission LP 590). A Sony DXC-960MD 3CCD color video camera was mounted on the microscope via a $2.5\times$ camera mount from Zeiss. The CCD camera was attached to a Matrox Marval G200 AGP frame grabber. Digital recordings were acquired at a frame rate of 15 frames/s. For the well with a radius of 100 $\mu$m, the acquired image sequence after cropping and resampling was $I(x,y,t)=420\times416\times2849$ voxels. The spatial sampling density was 1.92 samples/$\mu$m or one pixel per 0.52 $\mu$m, which is about a microsphere diameter. For the well with a radius of 150 $\mu$m, the acquired image sequence after cropping and resampling was $I(x,y,t)=473\times384\times3618$ voxels.

The spatial sampling density was 1.29 samples/$\mu$m. In both cases the acquisition started when the meniscus was convex. The instant $t=0$ corresponding to a flat meniscus was at frame 711 for the 100-$\mu$m well and at frame 513 for the 150-$\mu$m well. Microarrays with different sized wells were etched in silicon dioxide at DIMES (Delft Institute for Microelectronics and Submicron Technology). The calculations were performed with the MATLAB toolbox DIPimage [14].


[1] A. Lambacher and P. Fromherz, Appl. Phys. A **63**, 207 (1996).

[2] L.v.d. Doel and L.v. Vliet, Appl. Opt. **40**, 4487 (2001).

[3] R. Deegan, O. Bakajin, T. Dupont, G. Huber, S. Nagel, and T. Witten, Nature (London) **389**, 827 (1997).

[4] R. Deegan, O. Bakajin, T. Dupont, G. Huber, S. Nagel, and T. Witten, Phys. Rev. E **62**, 756 (2000).

[5] A. Einstein, Ann. Phys. (Leipzig) **17**, 549 (1905).

[6] I. Young, R. Zagers, L. v. Vliet, J. Mullikin, F. Boddeke, and H. Netten, in *Proceedings of the Eighth Scandinavian Conference on Image Analysis*, edited by K. Høgda, B. Braathen, and K. Heia (Norwegian Society for Image Processing and Pattern Recognition, Tromsø, Norway, 1993), pp. 493–498.

[7] J. Westerweel, Meas. Sci. Technol. **8**, 1379 (1997).

[8] C. Willert and M. Gharib, Exp. Fluids **10**, 181 (1991).

[9] B. Lucas and T. Kanade, in *Proceedings of the Seventh International Conference on Artificial Intelligence*, edited by P. Hayes (William Kaufmann, Vancouver, B.C., Canada, 1981), pp. 674–679.

[10] J. Canny, IEEE Trans. Pattern Anal. Mach. Intell. **8**, 679 (1986).

[11] D. Marr and E. Hildreth, Proc. R. Soc. London, Ser. B **207**, 187 (1980).

[12] W. Freeman and E. Adelson, IEEE Trans. Pattern Anal. Mach. Intell. **13**, 891 (1991).

[13] G. Granlund and H. Knutsson, *Signal Processing for Computer Vision* (Kluwer Academic, Dordrecht, 1995), Chap. 6.

[14] See http://www.ph.tn.tudelft.nl/DIPlib